

JGR Space Physics

RESEARCH ARTICLE

10.1029/2019JA027275

This article is a companion to Ergun et al. (2019) <https://doi.org/10.1029/2019JA027228>.

Key Points:

- Drift waves are potentially important in governing 3D structure of subsolar magnetic reconnection and in generating turbulence
- Drift waves displace or corrugate the current sheet and potentially displace the electron diffusion region of magnetic reconnection
- Parallel electric fields arise in the drift waves

Correspondence to:

R. E. Ergun,
ree@lasp.colorado.edu

Citation:

Ergun, R. E., Hoilijoki, S., Ahmadi, N., Schwartz, S. J., Wilder, F. D., Drake, J. F., et al. (2019). Magnetic reconnection in three dimensions: Modeling and analysis of electromagnetic drift waves in the adjacent current sheet. *Journal of Geophysical Research: Space Physics*, 124, 10,085–10,103. <https://doi.org/10.1029/2019JA027275>

Received 8 AUG 2019

Accepted 1 NOV 2019

Accepted article online 21 NOV 2019

Published online 11 DEC 2019

Magnetic Reconnection in Three Dimensions: Modeling and Analysis of Electromagnetic Drift Waves in the Adjacent Current Sheet

R. E. Ergun^{1,2}, S. Hoilijoki², N. Ahmadi², S. J. Schwartz², F. D. Wilder², J. F. Drake³, M. Hesse⁴, M. A. Shay⁵, H. Ji^{6,7}, M. Yamada⁶, D. B. Graham⁸, P. A. Cassak⁹, M. Swisdak³, J. L. Burch¹⁰, R. B. Torbert^{10,11}, J. C. Holmes¹², J. E. Stawarz¹³, K. A. Goodrich¹⁴, S. Eriksson², R. J. Strangeway¹⁵, and O. LeContel¹⁶

¹Department of Astrophysical and Planetary Sciences, University of Colorado Boulder, Boulder, CO, USA, ²Laboratory of Atmospheric and Space Sciences, University of Colorado Boulder, Boulder, CO, USA, ³Department of Astronomy, University of Maryland, College Park, MD, USA, ⁴Birkeland Centre For Space Science, University of Bergen, Bergen, Norway, ⁵Department of Physics and Astronomy, University of Delaware, Newark, DE, USA, ⁶Princeton Plasma Physics Laboratory, Princeton, NJ, USA, ⁷Department of Astrophysical Sciences, Princeton University, Princeton, NJ, USA, ⁸Swedish Institute of Space Physics, Uppsala, Sweden, ⁹Department of Physics and Astronomy, West Virginia University, Morgantown, WV, USA, ¹⁰Southwest Research Institute, San Antonio, TX, USA, ¹¹Department of Physics, University of New Hampshire, Durham, NH, USA, ¹²Space Research Institute, Austrian Academy of Sciences, Graz, Austria, ¹³Blackett Laboratory, Imperial College London, London, United Kingdom, ¹⁴Space Sciences Laboratory, University of California, Berkeley, CA, USA, ¹⁵IGGP, University of California, Los Angeles, CA, USA, ¹⁶Laboratoire de Physique des Plasmas, Palaiseau, France

Abstract We present a model of electromagnetic drift waves in the current sheet adjacent to magnetic reconnection at the subsolar magnetopause. These drift waves are potentially important in governing 3-D structure of subsolar magnetic reconnection and in generating turbulence. The drift waves propagate nearly parallel to the X line and are confined to a thin current sheet. The scale size normal to the current sheet is significantly less than the ion gyroradius and can be less than or on the order of the wavelength. The waves also have a limited extent along the magnetic field (\mathbf{B}), making them a three-dimensional eigenmode structure. In the current sheet, the background magnitudes of \mathbf{B} and plasma density change significantly, calling for a treatment that incorporates an inhomogeneous plasma environment. Using detailed examination of Magnetospheric Multiscale observations, we find that the waves are best represented by series of electron vortices, superimposed on a primary electron drift, that propagate along the current sheet (parallel to the X line). The waves displace or corrugate the current sheet, which also potentially displaces the electron diffusion region. The model is based on fluid behavior of electrons, but ion motion must be treated kinetically. The strong electron drift along the X line is likely responsible for wave growth, similar to a lower hybrid drift instability. Contrary to a classical lower hybrid drift instability, however, the strong changes in the background \mathbf{B} and n_o , the normal confinement to the current sheet, and the confinement along \mathbf{B} are critical to the wave description.

1. Introduction

Observations of magnetic reconnection at the Earth's magnetopause regularly indicate nearby strong wave activity and/or turbulence (e.g., Eastwood et al., 2009), particularly at the magnetopause current sheet adjacent to the electron diffusion region (EDR) on the magnetosphere side (Burch et al., 2016; Chen et al., 2017; Ergun et al., 2017). This turbulence or activity appears as strong fluctuations in the magnetic field (\mathbf{B}) and particle density (n) and may be a result from the unstable current sheet adjacent to the magnetic reconnection region (e.g., Daughton, 2003; Daughton et al., 2004; Daughton et al., 2011; Ergun et al., 2017; Ji et al., 2004, 2005; Karimabadi et al., 2007; Lapenta et al., 2006; Le et al., 2018; Nakamura et al., 2016; Price et al., 2016, 2017; Roytershteyn et al., 2012, 2013). These instabilities are of importance as they may influence the magnetic reconnection evolution and influence the three-dimensional (3-D) structure of magnetic reconnection.

Observations made by the Magnetospheric Multiscale (MMS) mission (Burch et al., 2016) are now able to determine more exact locations and the details of the current sheet instabilities relative to the EDR and thus help identify their role in magnetic reconnection. These observations indicate that many of the plasma

waves that have been associated with magnetic reconnection lie on the separatrix and are not in or immediately adjacent to the EDR (e.g., Le Contel, Retinò et al., 2016; Wilder et al., 2017). Basically, there appears to be paucity of wave activity inside of the EDR in many of the EDR events reported from MMS.

Waves with frequencies (f) between the ion cyclotron frequency (f_{ci}) and the lower hybrid frequency (f_{lh}), however, have been detected in the current sheet immediately adjacent to the EDR (Chen et al., 2017; Ergun et al., 2017) and have been seen in simulations (Daughton, 2003; Lapenta et al., 2006; Pritchett et al., 2012; Roytershteyn et al., 2012; Price et al., 2016; Price et al., 2017; Le et al., 2018). In this article, these waves are labeled “electromagnetic drift waves” (e.g., Ji et al., 2005) since they have a clear magnetic signature, appear to be confined to a thin current sheet (Ergun et al., 2017), and cause the current sheet to corrugate. Electromagnetic drift waves are potentially important as they appear to displace current sheet normal to its surface and may displace or influence the EDR (Ergun et al., 2019; hereafter called the *companion paper*). The emphasis of this article is to model these waves in detail and better understand the origin of the turbulence surrounding subsolar magnetic reconnection and the 3-D structure of magnetic reconnection.

The current sheet in the magnetosphere adjacent to asymmetric magnetic reconnection is observed to be only a few electron skin depths (λ_e) in width (e.g., Ergun et al., 2017), which is significantly less than the ion gyroradius (ρ_i) but many times the electron gyroradius (ρ_e). Simulations predict a similar thin current sheet (Cassak & Shay, 2007; Hesse et al., 2014). A primary characteristic of such thin current sheets is that a normal electric field (E_x , where x is normal to the current sheet) is required to balance the ion pressure (P_i) (Cassak & Shay, 2007; Hesse et al., 2014; Malakit et al., 2013). The resulting electron $\mathbf{E} \times \mathbf{B}$ drift produces the primary current (\mathbf{J}). Inside of the current sheet, generalized Ohm's law is dominated by the Hall term, $\mathbf{E} \approx \mathbf{J} \times \mathbf{B}/en$, so we label it as a “Hall” current sheet. The background values of \mathbf{B} and n change considerably making the local plasma environment strongly inhomogeneous. It is in this plasma environment that the electromagnetic drift waves reside (Ergun et al., 2017).

For many decades, instabilities in thin current sheets have been recognized and intensively investigated in studies of shocks and magnetic reconnection (e.g., Davidson et al., 1977; Davidson & Gladd, 1975; Huba et al., 1977; Krall & Liewer, 1971; Wu et al., 1983). These instabilities are often linked to wave modes seen in homogeneous plasmas such as ion acoustic waves, lower hybrid waves, and electron cyclotron waves. Many of these studies have concentrated on the lower-hybrid drift instability (LHDI, Krall & Liewer, 1971; Davidson & Gladd, 1975; Davidson et al., 1977). The LHDI is often associated with a gradient in electron pressure (∇P_e) or ion pressure (∇P_i) that results in a relative drift between the two species. If the density gradient is small, the LHDI develops primarily as electrostatic emissions with frequencies near f_{lh} . Daughton (2003) showed that a LHDI-like process in current sheets with a thickness (L_x) of $\sim \rho_i$ can result in longer-wavelength electromagnetic waves ($\lambda \approx \sqrt{\rho_i \rho_e}$) that have $f < f_{lh}$, propagate perpendicular to \mathbf{B} ($k_{\parallel} \sim 0$), are an eigenmode of (localized to) the current sheet, and are driven by ∇P_e . These results appear to have many similar characteristics to the observed electromagnetic drift waves. Our study extends the research of current sheet instabilities to waves that are more strongly confined ($L_x < \rho_i$), have negligible ∇P_e , and have a significant k_{\parallel} . Laboratory observations and theoretical analysis of electromagnetic drift waves (Ji et al., 2004; Ji et al., 2005) suggest that the behavior parallel to \mathbf{B} ($k_{\parallel} \neq 0$) is important. The latter study may be applicable to the MMS observations.

In this article, we develop an empirical model of an electromagnetic drift wave that is derived from observations of unstable current sheets that are adjacent to the EDR (Chen et al., 2017; Ergun et al., 2017; *companion paper*). The model is based on a fluid electron description in which the electrons are primarily frozen-in ($\mathbf{E} + \mathbf{V}_e \times \mathbf{B} \approx \mathbf{0}$) while the ions are treated as unmagnetized. We find that the wave consists of a series of electron flow vortices inside of the current sheet that propagate in the direction of the $\mathbf{E} \times \mathbf{B}$ electron drift. A significant find is that while a fluid description can be used for the electron motion, the ion motion normal to the current sheet surface dominates the ion density fluctuations and requires kinetic modeling.

A primary conclusion of this article is that the behavior along \mathbf{B} ($k_{\parallel} \neq 0$ or confinement along \mathbf{B}) and the inhomogeneous plasma conditions in the observed Hall current sheet considerably alter the wave dispersion from the classic LHDI, requiring a deeper investigation. The electromagnetic oscillations in an inhomogeneous plasma, the steep gradients in \mathbf{B} and n , and the confinement of \mathbf{E} and \mathbf{J} to a narrow region in the direction normal to the current sheet (L_x) must be included in studying the current sheet instabilities and

turbulence that are observed by MMS. The ion motion normal to the current sheet is critical to the development of the transverse electromagnetic wave and the eigenmode structure. Electron motion along the \mathbf{B} may be required to maintain a quasi-neutral plasma, which may cause strong, localized E_{\parallel} events.

Wave growth appears to come from the relative drift motion between the electrons and ions. If so, the electric field component along the electron drift (E_y) mediates the wave growth as in the LHDI. Basically, the electromagnetic drift wave appears to require both the normal component of the electric field (E_x), which influences the real part of the wave dispersion, and a component along the primary current (E_y) that enables wave growth.

2. An Empirical Model of an Electromagnetic Drift Wave in a Current Sheet

2.1. A 2-D Empirical Model

Four electromagnetic drift wave events near an EDR are described in the *companion paper*, so we refer the reader to that article for observational details. Figure 1 displays an electromagnetic drift wave detected by MMS1 on 14 December 2015 (Chen et al., 2017; Ergun et al., 2017), which is Event A in the *companion paper*. The mission and the instruments are described in a series of published articles (Burch, Moore, et al., 2016; Ergun, Tucker, et al., 2016; Le Contel, Leroy, et al., 2016; Lindqvist et al., 2016; Pollock et al., 2016; Russell et al., 2016; Torbert et al., 2016). The vector values in Figure 1 are plotted in coordinates that are usually labeled “LMN” (see Denton et al., 2018). In this article, we use coordinates X , Y , and Z to make analytic formulas readable. A simple mapping calls for X in the direction normal to the current sheet (N , minimum variance), Z in the direction along the reversing magnetic field (L , maximum variance), and Y makes a right-handed coordinate system ($-M$), which often is along the X line of magnetic reconnection. For this investigation, we choose a coordinate system that is optimized for the current sheet rather than for the EDR of magnetic reconnection (Chen et al., 2017). The coordinate transformation is written in Figure 1i. This coordinate system retains nearly the same normal direction (X or N) as that derived by (Chen et al., 2017). However, Y ($-M$) and Z (L) are rotated by $\sim 20^\circ$ about the normal. This rotation is such that Z is nearly parallel to \mathbf{B} , so that one can better distinguish the parallel and perpendicular properties of the drift waves.

The top panel (Figure 1a) displays the three components of \mathbf{B} . The EDR (Chen et al., 2017) is marked in the figure. The electron and ion densities are plotted in Figure 1b. The oscillations from the drift wave are visible in \mathbf{B} and the electron density (n_e) from $\sim 01:17:39.8$ to $\sim 01:17:40.2$ UT. The ion density is sampled at a lower rate, so the oscillations are not detected. In this event, the MMS spacecraft traverse a current sheet that is adjacent to an EDR at a speed of ~ 40 km/s (*companion paper*). The variations of \mathbf{B} and n are consistent with a displacement of the current sheet in the X direction. In other words, the perturbation in B_z can be represented by $\tilde{B}_z \cong \partial \bar{B}_z / \partial x \xi$, and the perturbation in n_e can be represented by $\tilde{n}_e \cong \partial \bar{n}_e / \partial x \xi$ with ξ representing a common displacement in the X direction. In this article, all values with a tilde, for example, \tilde{B}_z , represent the oscillatory behavior at the wave frequency whereas values topped with a bar, for example, \bar{B}_z , represent the background value such that $B_z = \bar{B}_z + \tilde{B}_z$. For convenience, we use n_o to represent either \bar{n}_i or \bar{n}_e .

The next six panels, Figures 1c–1h, plot, in order, \tilde{B}_z , \tilde{n}_e , \tilde{E}_x , \tilde{E}_y , \tilde{J}_x , and \tilde{J}_y . The time series data are each filtered to a bandpass from 5 to 10 Hz to isolate the ~ 7.5 Hz signals of the drift wave. There are five vertical dashed lines to represent instances of the wave phase in \tilde{B}_z and \tilde{n}_e at 180° intervals. The times marked t_1 through t_9 represent 90° intervals in phase.

Clearly, \tilde{B}_z and \tilde{n}_e are $\sim 180^\circ$ out of phase (Ergun et al., 2017). \tilde{J}_x shows a 90° phase lag from \tilde{B}_z . \tilde{E}_y has a slightly smaller phase lag. \tilde{E}_x and \tilde{J}_y appear to have a poor phase relation with \tilde{B}_z . The background values, \bar{E}_x and \bar{J}_y , are strongly peaked in the current sheet, so if an oscillatory displacement of \bar{E}_x is the source of \tilde{E}_x , a phase reversal is expected to occur in \tilde{E}_x (and \tilde{J}_y) as the MMS1 spacecraft passes through the current sheet (see Figure 1e). The relative locations of the MMS satellites are depicted in the lower left corner of Figure 1i. The plasma conditions and the coordinate transformation are written in Figure 1i.

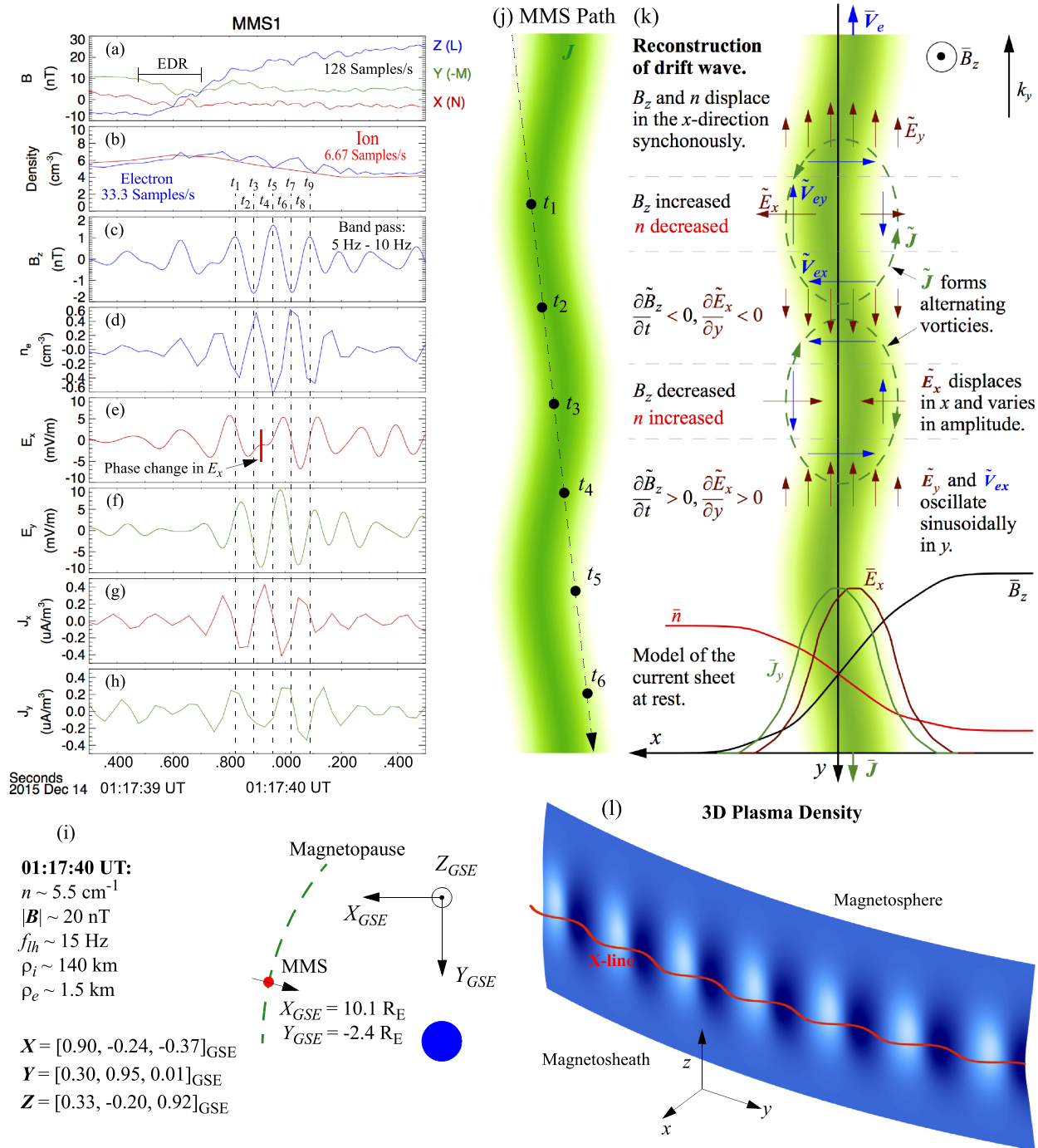


Figure 1. Observations and model of an electromagnetic drift wave. (a) The magnetic field in rotated coordinated coordinates, which are detailed in panel (i). (b) The plasma densities measured by the FPI instrument. The ion density is at a lower cadence than the electron density, so waves may not appear. (c) B_z in the frequency band from 5 to 10 Hz. The vertical dashed lines mark the peaks and minimums of B_z during the electromagnetic drift wave. The electromagnetic drift wave appears from ~01:07:39.8 to ~01:07:40.2 UT. (d) n_e in the frequency band from 5 to 10 Hz. (e) and (f) E_x and E_y in the frequency band from 5 to 10 Hz. E_x undergoes a phase change as MMS1 crosses through the center of the current sheet. (g and h) J_x and J_y in the frequency band from 5 to 10 Hz. (i) The relative position of the MMS satellites. Written on the panel are the plasma conditions in the center of the electromagnetic drift wave and the coordinate transformation to a surface-normal coordinate system. (j) The apparent MMS path through the drift wave. The dots and times correspond to the peaks and valleys of B_z . (k) A reconstruction of the electromagnetic drift wave with common features from four events studied in the companion paper. The drift wave appears to be comprised of a series of electron flow vortices (current vortices) that alternate in sense that result in the corrugation of the current sheet. It is important to recognize that E_x develops from the combination of current sheet displacement and amplitude modulation. A model of the static current sheet is at the bottom. (l) A 3-D rendering of the electron density corrugation associated with the electromagnetic drift wave. The electromagnetic drift wave is confined in X and in Z and may displace the X line.

The right side of Figure 1k displays a model of the electromagnetic drift wave in a two-dimensional plane. The model is based on the phase relations of \tilde{B}_z , \tilde{n}_e , \tilde{E}_x , \tilde{E}_y , \tilde{J}_x , and \tilde{J}_y from this event and from three other events in the *companion paper*. In the center of Figure 1j is a conceivable path of MMS1 that includes the wave propagation. The lower right corner of Figure 1l contains a 3-D rendering of the electron density corrugation of the drift wave that is confined in both X and Z . The confinement in Z is discussed in section 3.

In developing this model, electrons are considered to be frozen-in ($\mathbf{E} + \mathbf{V}_e \times \mathbf{B} \approx 0$). To the contrary, ions are treated as unmagnetized. The foundation of the drift wave appears to be a series of vortices in $\tilde{\mathbf{J}}$ that alternate in sense, clockwise then counterclockwise. The vortices are superimposed on a strong constant current (\tilde{J}_y) of the current sheet. The existence of the vortices is supported by a detailed examination $\tilde{\mathbf{E}}$ and $\tilde{\mathbf{J}}$ in four separate events. When counterclockwise (Figure 1 at t_1), the $\tilde{\mathbf{J}}$ vortices are coincident with an increase in \tilde{B}_z and when clockwise (Figure 1 at t_3), they are coincident with a decrease \tilde{B}_z .

The wave vector (k_y) in Figure 1 (right) is negative reflecting the propagation direction of the wave. Importantly, the observations indicate that the drift wave is strongly confined to the current sheet in the X direction with a characteristic size of $L_x \sim 10$ km. The drift waves are thus confined to a region with a strong gradient in the background magnetic field, $\partial \tilde{B}_z / \partial x$, and a strong gradient in the background density, $\partial \tilde{n}_e / \partial x$. The drift wave is primarily electrostatic but has a significant electromagnetic contribution as $\partial \tilde{\mathbf{B}} / \partial t$ is observed. The observations also show that there is a significant parallel contribution (not shown in Figure 1; see section 3). Thus, variations in the Z direction must be part of the wave description.

2.2. Wavelength Determination

The wavelength and wave speed of the drift waves are critical since they will guide our subsequent analysis and have been a subject of debate (Graham et al., 2017). In this section, we discuss four ways to determine the wavelength, two of which are from time delays in the observations. The other two methods employ Maxwell's equations.

The top panel in Figure 2a displays $|\mathbf{B}|$ from the four MMS spacecraft. MMS1 entered the current sheet before the other three. As such, the wave phase speed is estimated at the end of the event as observed on MMS1 when all four spacecraft are in the current sheet at the same time. The correlations between the $\tilde{\mathbf{B}}$ signals (Figure 2b), filtered to a bandpass of 5 to 10 Hz, indicate a wave speed (written to the right of Figure 2b) greater than ~ 300 km/s, even under the uncertainties in time delays. The direction is primarily in $-Y$ (M). Uncertainties in the velocity estimates are displayed on the plot. An estimate using only three spacecraft in this same time period (MMS2, MMS3, and MMS4) and assuming a steady value of $V_x = 40$ km/s (Figure 2c) indicated a wave speed of roughly 600 km/s with a factor of 2 uncertainty, primarily in the $-Y$ GSE direction (Ergun et al., 2017). A second way to estimate k_y is from probe-to-probe delays (*companion paper*), which also support a wave phase speed of roughly 350 km/s, albeit with a factor of 2 uncertainty.

A third method to estimate wave phase speed or wavelength is through the use of Ampère's law with observations of \tilde{J}_x from \tilde{B}_z (Norgren et al., 2012), which often works well for lower hybrid waves. Since $\nabla \times \mathbf{B} = \mu_o \mathbf{J}$, one can deduce that a purely perpendicular wave ($k_z = 0$) would obey:

$$|k_y| |\tilde{B}_z| \approx \mu_o |\tilde{J}_x| \quad (1)$$

Quantitatively, the measured values of $|\tilde{J}_x|$ ($\sim 0.5 \mu\text{A m}^{-2}$) and $|\tilde{B}_z|$ (~ 1.65 nT) suggest a phase speed (v_ϕ) of ~ 130 km/s with a wavelength (λ) of ~ 17 km. The wavelength derived from Ampère's law is roughly 1/3 of that suggested from the observations. However, there are two possible sources of error in using this method. In this case, there may be a significant contribution from $\partial \tilde{B}_y / \partial z$ since \mathbf{B} may have curvature (Figure 2d). Alternatively, the measurement of \tilde{J}_x includes only the electron current (ions are undersampled), so an ion current in the X direction may alter the result. The latter source of error is shown to be small.

Another way to determine k_y and v_ϕ is to use the Z component of Faraday's law, $\nabla \times \mathbf{E} = -\partial \tilde{\mathbf{B}} / \partial t$, which implies that

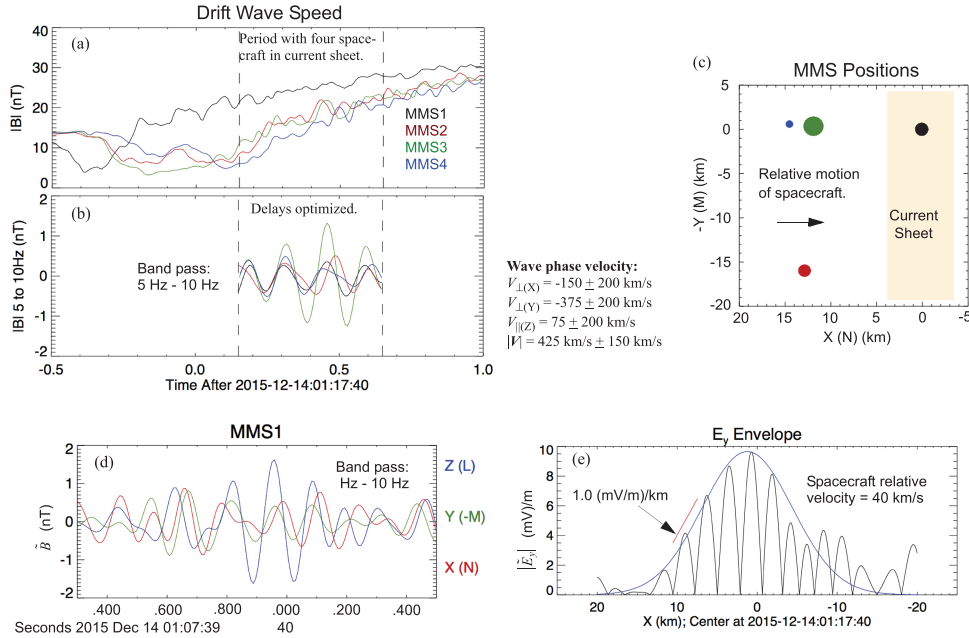


Figure 2. Calculation of wave phase velocity for 14 December 2015 event. (a) $|B|$ from the four MMS spacecraft. The colors represent the spacecraft. (b) $|B|$ from all four MMS spacecraft. The data have been filtered to a frequency band of 5 to 10 Hz. The times are shifted to align the signals to MMS1. To the right are the calculated phase velocities. (c) The relative positions of the MMS spacecraft during the event. (d) B signals filtered to a frequency band of 5 to 10 Hz. Since B is in the Z direction, B_z represents amplitude modulations. B_y and B_x indicate that the magnetic field is curved. (e) $|E_y|$ shows a narrow confinement of the drift wave. $|\partial \tilde{E}_y / \partial x|$ is approximately 10^{-6} V/m² given that the spacecraft has a relative velocity to the current sheet of 40 km/s.

$$-ik_y \tilde{E}_x + \frac{\partial \tilde{E}_y}{\partial x} = i\omega \tilde{B}_z \quad (2)$$

One must examine the envelope of \tilde{E}_y as a function of distance across the current sheet in Figure 2e, which reveals a narrowly confined wave. Using the observations, we get

$$|\tilde{E}_x| \approx 6 \times 10^{-3} \frac{\text{V}}{\text{m}}, \quad \left| \frac{\partial \tilde{E}_y}{\partial x} \right| \approx 10^{-6} \frac{\text{V}}{\text{m}^2}, \quad \text{and} \quad |\omega \tilde{B}_z| \approx 8 \times 10^{-7} \frac{\text{V}}{\text{m}^2} \quad (3)$$

which implies that

$$|k_y| = \frac{1}{|\tilde{E}_x|} \left| i\omega \tilde{B}_z - \frac{\partial \tilde{E}_y}{\partial x} \right| \approx 1.5 \times 10^{-4} \text{ m}^{-1} \quad (4)$$

Under this calculation, $\lambda \sim 40$ km and $v_\phi \sim 300$ km/s, which are close to the values suggested by the observations. Given the uncertainties, the excellent agreement between the wavelength derived from the observations and the wavelength derived from Faraday's law is likely coincidental. The Faraday's law method of determining k_y and v_ϕ is also subject to error, primarily in determining the phase between $\partial \tilde{E}_y / \partial x$ and $i\omega \tilde{B}_z$. However, given the relatively small value of $i\omega \tilde{B}_z$ the uncertainty and low uncertainty in measuring $\partial \tilde{E}_y / \partial x$, the wave speed has a roughly 25% uncertainty. Since the measured amplitude of \tilde{B}_y is similar to that of \tilde{B}_z , $\partial \tilde{B}_y / \partial z$ appears to be significant. We find that in this particular event, the use of the Faraday's law gives a better estimate of the wavelength than does the use of Ampère's law (Graham et al., 2017). We use $\lambda \sim 40$ km and $v_\phi \sim 300$ km/s in our analysis.

2.3. Lower Hybrid Waves

A unique feature of the events that we analyze is that the oscillations are in a thin (Hall) current sheet, which calls for a 3-D eigenmode treatment. Because such a treatment is particularly complicated, we begin by examining lower hybrid waves. In the simplest form of the lower hybrid wave, ions have an inertial response and electrons have a polarization drift:

$$\frac{\partial \tilde{V}_{iy}}{\partial t} = \frac{e\tilde{E}_y}{m_i} \quad (5)$$

$$\tilde{V}_{ey} = -\frac{m_e}{eB^2} \frac{\partial \tilde{E}_y}{\partial t} \quad (6)$$

where m_i is the ion mass, m_e is the electron mass, and e is the fundamental charge. \mathbf{B} is assumed to be in the Z direction. The continuity equations

$$\frac{\partial n_i}{\partial t} + \nabla \cdot (n_i \mathbf{V}_i) = 0 \quad (7)$$

$$\frac{\partial n_e}{\partial t} + \nabla \cdot (n_e \mathbf{V}_e) = 0 \quad (8)$$

can be simplified by assuming a plane wave ($\sim e^{i(k_y y - \omega t)}$) with frequency ω and a wave vector (k_y) purely in the Y direction. We assume, for now, a homogeneous plasma. We also assume that the wave perturbations, \tilde{n}_i , \tilde{n}_e , \tilde{V}_{iy} , \tilde{V}_{ey} , and \tilde{E}_y , are small. By ignoring second order terms, the resulting density perturbations are as follows:

$$\tilde{n}_i = \frac{k_y}{\omega} n_o \tilde{V}_{iy} = \frac{ik_y n_o e \tilde{E}_y}{\omega^2 m_i} \quad (9)$$

$$\tilde{n}_e = \frac{k_y}{\omega} n_o \tilde{V}_{ey} = \frac{ik_y n_o m_e \tilde{E}_y}{e B_z^2} \quad (10)$$

Assuming a quasi-neutral plasma ($\tilde{n}_i \approx \tilde{n}_e$), which is undoubtedly satisfied since $\omega < \omega_{pi}$ (where ω_{pi} is the ion plasma frequency), one gets the well-established result that $\omega = \sqrt{\omega_{ci} \omega_{ce}}$, where ω_{ci} is the ion cyclotron frequency ($e|\mathbf{B}|/m_i$) and ω_{ce} is the electron cyclotron frequency ($e|\mathbf{B}|/m_e$).

However, if when examining the observations carefully (Figure 1 right), one can deduce that the ions do not have an inertial response and further analysis shows that the electron polarization drift is negligible. The inferred ion density perturbations (assuming a quasi-neutral plasma) are 180° out of phase with the inertial ion motion predicted by a classical (electrostatic in cold plasma) lower hybrid wave. The primary reason is that the drift wave frequencies are significantly below the lower hybrid frequency (ω_{lh}) and the phase velocities of the waves are near the thermal velocity of the ions ($V_{thi} = \sqrt{T_i/m_i}$ where T_i is the ion temperature), so the ion susceptibility (χ_i) is not inertial. For an inertial response, $\omega^2 \gg \gamma_i k^2 v_{thi}^2$ which gives

$$\chi_i = -\frac{\omega_{pi}^2}{\omega^2} \quad (11)$$

whereas for a thermal response $\omega^2 \ll \gamma_i k^2 v_{thi}^2$ so

$$\chi_i = \frac{\omega_{pi}^2}{\gamma_i k^2 v_{thi}^2} \quad (12)$$

γ_i is the polytropic constant. In the 14 December 2015 event, $T_i \sim 600$ eV so $v_{thi} \sim 250$ km/s, which is comparable to the wave speed. We find the same result in many other events that we have examined, $\omega^2 \approx \gamma_i k^2 v_{thi}^2$ using the best estimates of k_y . As such, the imaginary contribution from χ_i must be considered and, in some cases, dominates the ion response.

2.4. Electron Motion Perpendicular to \mathbf{B} in Density and Magnetic Field Gradients

The observed drift waves need to be treated in 3-D and in an inhomogeneous plasma environment. In this section, we examine the perpendicular motion of the electrons in the drift wave with significant $\partial \tilde{B}_z / \partial x$ and $\partial \tilde{n}_e / \partial x$. We assume a background electron drift (\tilde{V}_{ey}). The electron motion can be approximated by assuming that the electrons are frozen in ($\mathbf{E} + \mathbf{V}_e \times \mathbf{B} \approx 0$). However, we show later that the observed density perturbations (\tilde{n}_e) suggest that $\nabla \tilde{P}_e$ is finite but small, so electron cross-field transport may be possible. To start, we ignore $\nabla \tilde{P}_e$ and have a more involved discussion of the parallel motion in section 3.

The linearized electron continuity equation involves all three components:

$$\frac{\partial n_e}{\partial t} + \nabla \cdot (n_e \mathbf{V}_e) = 0 \implies i\omega \tilde{n}_e = \frac{\partial n_o}{\partial x} \tilde{V}_{ex} + n_o \nabla \cdot \tilde{\mathbf{V}}_e + ik_y \tilde{n}_e \bar{V}_{ey} \quad (13)$$

which reduces to

$$\frac{\tilde{n}_e}{n_o} = \frac{-i}{\omega - k_y \bar{V}_{ey}} \left(\frac{1}{n_o} \frac{\partial n_o}{\partial x} \tilde{V}_{ex} + \nabla \cdot \tilde{\mathbf{V}}_e \right) \quad (14)$$

Observations indicate that the contribution from $\nabla \cdot \tilde{\mathbf{V}}_e$ may be finite but does not dominate since the flow is primarily in a vortex. Therefore, \tilde{n}_e predominantly results from a density gradient, $\partial n_o / \partial x$, combined with motion in the X direction as observed (see *companion paper*). As a result, \tilde{n}_e is dominated by \tilde{E}_y and the phase of \tilde{n}_e is 90° advanced from \tilde{E}_y , which is seen in the observations and depicted in the model (Figure 1).

The gradient in \bar{B}_z is equally as important. One can expand equation (14) by rewriting it in the form:

$$\frac{\tilde{n}_e}{n_o} = \frac{-i}{\omega - k_y \bar{V}_{ey}} \left(\frac{1}{n_o} \frac{\partial n_o}{\partial x} \tilde{V}_{ex} \right) - \frac{i}{\omega - k_y \bar{V}_{ey}} \left(\frac{\partial \tilde{V}_{ex}}{\partial x} + \frac{\partial \tilde{V}_{ey}}{\partial y} \right) - \frac{i}{\omega - k_y \bar{V}_{ey}} \frac{\partial \tilde{V}_{ez}}{\partial z} \quad (15)$$

If electrons are frozen in then

$$E_x = -V_{ey} B_z + V_{ez} B_y, E_y = V_{ex} B_z - V_{ez} B_x \quad (16)$$

Now apply Faraday's law ($\nabla \times \mathbf{E} = -\partial \mathbf{B} / \partial t$) in the Z direction and keep the lowest order oscillatory terms:

$$\frac{\partial \tilde{E}_y}{\partial x} - \frac{\partial \tilde{E}_x}{\partial y} = -\frac{\partial \tilde{B}_z}{\partial t} \implies \frac{\partial \tilde{V}_{ex}}{\partial x} \bar{B}_z + \tilde{V}_{ex} \frac{\partial \bar{B}_z}{\partial x} + \frac{\partial \tilde{V}_{ey}}{\partial y} \bar{B}_z + \bar{V}_{ey} \frac{\partial \tilde{B}_z}{\partial y} = -\frac{\partial \tilde{B}_z}{\partial t} \quad (17)$$

which becomes

$$\frac{\partial \tilde{V}_{ex}}{\partial x} + \frac{\partial \tilde{V}_{ey}}{\partial y} = i \frac{\bar{B}_z}{B_z} (\omega - k_y \bar{V}_{ey}) - \frac{\bar{V}_{ex}}{B_z} \frac{\partial \bar{B}_z}{\partial x} \quad (18)$$

The continuity equation (15) reduces to

$$\frac{\tilde{n}_e}{n_o} = \frac{-i \tilde{V}_{ex}}{\omega - k_y \bar{V}_{ey}} \left(\frac{1}{n_o} \frac{\partial n_o}{\partial x} - \frac{1}{\bar{B}_z} \frac{\partial \bar{B}_z}{\partial x} \right) + \frac{\bar{B}_z}{B_z} \frac{i}{\omega - k_y \bar{V}_{ey}} \frac{\partial \tilde{V}_{ez}}{\partial z} \quad (19)$$

The above equation mistakenly suggests that $\partial \bar{B}_z / \partial x$ may play a major role in driving the density perturbation. Observations show that \tilde{B}_z / \bar{B}_z has the same magnitude as \tilde{n}_e / n_o but has the opposite sign, which makes it difficult to draw conclusions from equation (19).

2.5. Electromagnetic Properties and Magnetic Field Perturbation

Here we investigate the electromagnetic component of the drift waves by examining the oscillations in $B_z = \bar{B}_z + \tilde{B}_z$. We start by examining Faraday's law with frozen-in electrons:

$$\frac{\partial B_z}{\partial t} = -(\nabla \times \mathbf{E})_z = \frac{\partial E_x}{\partial y} - \frac{\partial E_y}{\partial x} = -\frac{\partial (B_z V_{ey})}{\partial y} - \frac{\partial (B_z V_{ex})}{\partial x} \quad (20)$$

Expanding the right-hand side of equation (20)

$$\frac{\partial B_z}{\partial t} = - \left(V_{ey} \frac{\partial B_z}{\partial y} + V_{ex} \frac{\partial B_z}{\partial x} \right) - B_z \left(\frac{\partial V_{ey}}{\partial y} + \frac{\partial V_{ex}}{\partial x} \right) \quad (21)$$

which reduces to

$$\frac{\partial B_z}{\partial t} = - \mathbf{V}_{e\perp} \cdot \nabla_{\perp} B_z - B_z (\nabla_{\perp} \cdot \mathbf{V}_{e\perp}) \quad (22)$$

Recalling that $V_{ey} = \bar{V}_{ey} + \tilde{V}_{ey}$ with $\partial \bar{V}_{ey} / \partial y = 0$ and keeping only lowest order oscillatory terms

$$-i\omega \tilde{B}_z = -ik_y \bar{V}_{ey} \tilde{B}_z - \tilde{V}_{ex} \frac{\partial \tilde{B}_z}{\partial x} - \tilde{B}_z (\nabla_{\perp} \cdot \tilde{\mathbf{V}}_{e\perp}) \quad (23)$$

which can be rewritten as follows:

$$\frac{\tilde{B}_z}{\bar{B}_z} = \frac{-i\tilde{V}_{ex}}{\omega - k_y \bar{V}_{ey}} \left(\frac{1}{\bar{B}_z} \frac{\partial \tilde{B}_z}{\partial x} \right) - \frac{i(\nabla_{\perp} \cdot \tilde{\mathbf{V}}_{e\perp})}{\omega - k_y \bar{V}_{ey}} \quad (24)$$

There are several important conclusions that one can draw from equation (24). As noted earlier, observations indicate that the contribution from $\nabla_{\perp} \cdot \tilde{\mathbf{V}}_{e\perp}$ may be finite but does not dominate since the flow is primarily in a vortex. Therefore, the observed magnetic field perturbations chiefly result from $\partial \tilde{B}_z / \partial x$ combined with motion in the X direction, while the observed density perturbations largely result from $\partial n_o / \partial x$ combined with the same motion in the X direction (equation (14)). Thus, the wave that creates \tilde{B}_z and \tilde{n}_e must be an eigenmode confined to the region of a strong but opposite gradient in n_o and \bar{B}_z . Ultimately, both \tilde{B}_z and \tilde{n}_e are dominated by \tilde{E}_y . Equations (14) and (24) combine to create the corrugation of the current sheet and explain the apparent transverse motion in the X or N direction that propagates in the $-Y$ or $+M$ direction.

2.6. Ion Susceptibility and Ion Motion in the Observed Drift Wave

In the observations, \tilde{n}_i is not directly measured (ions are under sampled) but quasi-neutrality dictates that $\tilde{n}_i \approx \tilde{n}_e$. Because $v_{\phi} \approx v_{thi}$, the ion motion in the Y direction (\tilde{V}_{iy}) must be treated with kinetic-based plasma physics. Figure 3a displays $\tilde{\chi}_i$ calculated numerically (Fried & Conte, 1961; also see Ergun, Holmes, et al., 2016) and compared to equations (11) and (12). Here χ_i is applicable only to the Y motion of the ions since $\partial n_o / \partial y$ can be neglected. Given the possible range of values of k_y , the imaginary part of χ_i appears to dominate. The real part of $\tilde{\chi}_i$ is positive (thermal response), which could result in a phase of \tilde{n}_i that is compatible with the observations. However, the calculated amplitude of the ion density perturbation from the real part of χ_i (and only the Y motion)

$$\left| \frac{\tilde{n}_i}{n_o} \right| = \left| \frac{\tilde{E}_y \chi_i' \epsilon_o k_y}{e} \right| \approx 1.5\% \quad (25)$$

is significantly lower than that seen from the observations ($\sim 10\%$ assuming quasi neutrality), so Y motion of ions (driven by E_y) cannot by itself explain \tilde{n}_i that is inferred from the observations.

In addition to the ion motion in the Y direction (\tilde{V}_{iy}), \tilde{V}_{ix} can be significant since $|\tilde{E}_x|$ and $|\tilde{E}_y|$ are nearly equal. The X motion, ignored in most treatments of the LHDI, requires a far more involved kinetic treatment due to the strong gradients in \bar{n}_i and \bar{T}_i . We study the X motion with a simple, one-dimensional test-particle treatment. Figure 3b displays the domain of the test-particle treatment, which extends ± 50 km in the X direction. The background parameters, \bar{n}_i , \bar{T}_i , and \bar{E}_x , are kinetically constructed to replicate the current sheet observations. Magnetosheath ions are injected on the left and ions from the magnetosphere are injected on the right. The ions are treated as unmagnetized, so \mathbf{B} is not considered.

After kinetically replicating the static current sheet, \bar{E}_x is displaced in the X direction under sinusoidal motion, $\xi = \xi_o \sin(\omega t)$, with $\xi_o = 8$ km (see *companion paper*; Figure 1k). The oscillatory displacement of

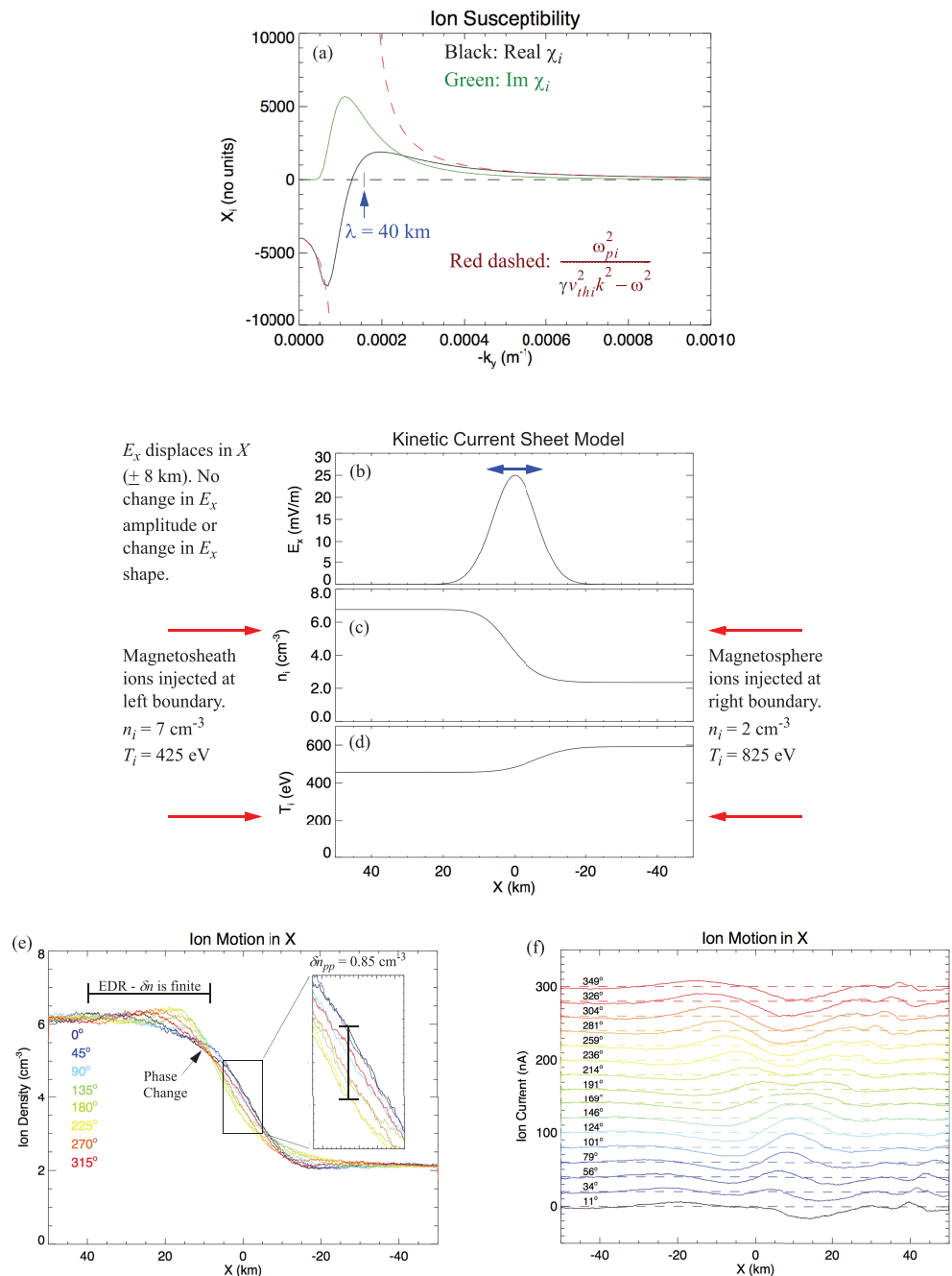


Figure 3. The ion susceptibility (χ_i) in the drift wave. (a) χ_i applicable for motion in the Y direction. The plasma is assumed to be homogeneous. Since $\omega/k_y \approx v_{thi}$, there is a strong imaginary response. (b–d) A static, kinetic model of the observed current sheet on 14 December 2015. \bar{E}_x is prescribed. In the kinetic model, magnetosheath ions are injected on the left side and magnetosphere ions on the right side. The resulting \bar{n}_i and \bar{T}_i are a close match to those observed. \bar{E}_x is displaced in the X-direction a distance of $\xi = \xi_o \sin(\omega t)$, with $\xi_o = 8$ km. (e) The ion density as a function of X. The colors represent wave phase. To lowest order, the ion density is displaced in the X direction. \bar{E}_x appears to “plow” the ions back and forth creating a significant \tilde{n}_i . In this example, the \tilde{n}_i lags \bar{E}_x motion by about 90° . (f) The ion currents as a function of wave phase. In this example, the peak ion currents are roughly 5% of the peak electron currents.

\bar{E}_x results in significant density perturbations ($|\tilde{n}_i|/n_o \sim 8\%$ in Figure 3e) dominated by apparent motion of \tilde{n}_i . However, the motion of \bar{E}_x and the motion of \tilde{n}_i are not phased the same as seen in the observations (Figure 1), so a simple motion in \bar{E}_x cannot replicate the proper phase of the \tilde{n}_i . By adding an amplitude

modulation in E_x (~ 10 mV/m) and changing the shape of E_x (not shown) one can better replicate the observations. However, such a replication is not unique. Figure 3f shows that the ion current reaches ~ 20 nA/m², which is roughly 5% of the electron current.

This rudimentary study of the kinetic response of the ions in \tilde{V}_{iy} and \tilde{V}_{ix} leads us to conclude that a combination of oscillatory displacement of E_x , amplitude modulation of E_x , and/or change in shape of E_x is required to the observed amplitude and phase of \tilde{n}_i . The \tilde{V}_{iy} motion is less effective but can contribute if χ_i is dominated by a thermal response. A kinetic treatment is required to fully understand the ion response.

Another important fact is that the phase velocity of the drift waves is very near the ion thermal velocity. Since $v_\phi \sim v_{thi}$, the ions undergo a strong Landau response or energy exchange. In the absence of a strong electron drift, this Landau resonance would generally lead to strong damping. However, because of the strong electron drift, the ion resonance (imaginary part of χ_i) may be part of a strong interaction between the electron and ions which may promote an instability.

3. A 3-D Empirical Model

3.1. Electromagnetic Properties Parallel to \mathbf{B}

While the 2-D analysis and model describes many of the characteristics of the drift wave, the significant field-aligned component to these waves is equally as important (*companion paper*; Figure 1e). One way to investigate the parallel propagation is by comparing the wave speed derived from Ampère's law to that derived from Faraday's law, as done in section 2.2. Faraday's law

$$-ik_y \tilde{E}_x + \frac{\partial \tilde{E}_y}{\partial x} = i\omega \tilde{B}_z \quad (26)$$

suggests with a $\sim 25\%$ uncertainty that $v_\phi \sim 300$ km/s and $\lambda \sim 40$ km ($k_y = 1.5 \times 10^{-4}$), which are close to those suggested by the observations. A reinvestigation of Ampère's law keeping all terms

$$\frac{\partial \tilde{B}_y}{\partial z} = \frac{\partial \tilde{B}_z}{\partial y} - \mu_0 \tilde{J}_x \quad (27)$$

indicates that $\partial \tilde{B}_y / \partial z$ must make a significant contribution to \tilde{J}_x . The measured \tilde{B}_y is ~ 1 nT compared to $\tilde{B}_z \sim 1.7$ nT in the observations. However, it is the derivative in the Z direction that is of importance.

The vortical motion of the electrons is a key consideration. Since electrons are primarily frozen in, \mathbf{B} must also rotate with the electrons. In addition, the wave is confined in the region of thin current sheet near the X line of magnetic reconnection, which is localized in X but also localized in the Z direction (Figure 4k) as shown in observations and simulations of magnetic reconnection at the magnetopause (e.g., Price et al., 2016; Price et al., 2017). The magnetic field rotation must be also confined along $\pm Z$ inside of the thin part of the current sheet.

Figure 4 replots the event on 14 December 2015 with additional values relevant to the parallel structure of the drift wave. The top four panels, Figures 4a–4d, replot Figure 1a–1d for reference and phase comparison. Figure 4e plots the ZZ component of the electron pressure tensor (\tilde{P}_{ezz}) filtered to the band pass of 5 to 10 Hz and Figure 4f plots the off-diagonal XZ term, \tilde{P}_{exz} , which is also filtered to the band pass of 5 to 10 Hz. The \tilde{P}_{exx} and \tilde{P}_{eyy} components show similar behavior as the \tilde{P}_{ezz} component with slightly lower amplitudes. The \tilde{P}_{eyz} term also displays a nonnegligible oscillation.

\tilde{E}_z is plotted in Figure 4g and the full band (DC to ~ 3 kHz) $E_{||}$ is plotted in Figure 4h. It is important to realize that \tilde{E}_z (from LMN coordinate system) is not exactly parallel to \mathbf{B} since the direction of \mathbf{B} oscillates by up to 10° and changes during the event whereas $E_{||}$ is derived from the instantaneous direction of \mathbf{B} . Figure 4i shows \tilde{J}_z filtered to the frequency band of 5–10 Hz, and Figure 4j plots $\mathbf{J} \cdot (\mathbf{E} + \mathbf{V}_e \times \mathbf{B})$ from DC to ~ 12 Hz.

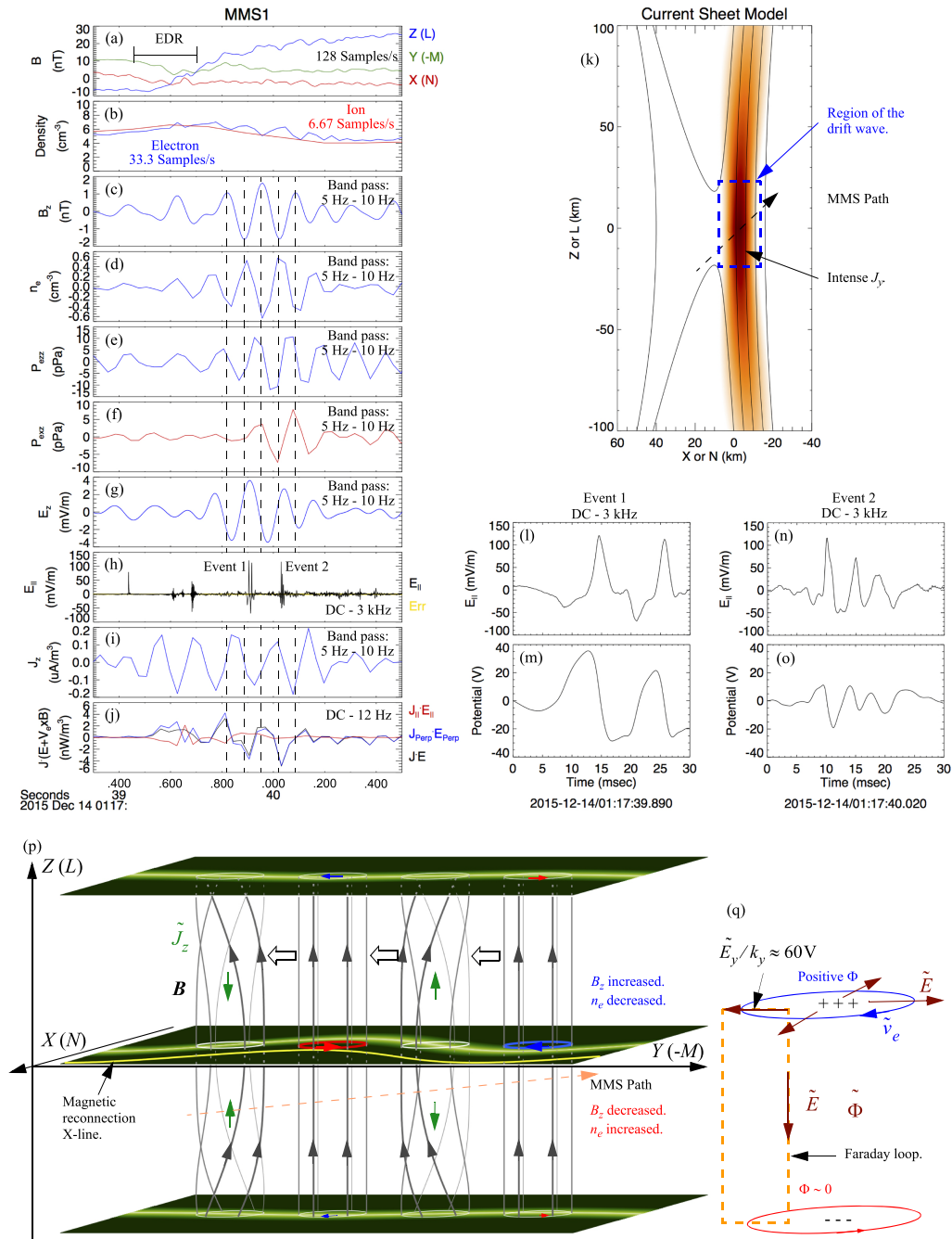


Figure 4. The parallel structure of the observed drift waves. (a) \mathbf{B} in coordinates relevant to the current sheet, which are detailed in Figure 1i. (b) The plasma densities measured by the FPI instrument. (c) B_z in the frequency band from 5 to 10 Hz. The vertical dashed lines mark the peaks and minimums of during the electromagnetic drift wave. (d) \tilde{n}_e in the frequency band from 5 to 10 Hz. (e) The ZZ component of the measured electron pressure tensor (\tilde{P}_{ezz}) in the frequency band from 5 to 10 Hz. (f) The XZ component of the measured electron pressure tensor (\tilde{P}_{ezx}) in the frequency band from 5 to 10 Hz. (g) \tilde{E}_z in the frequency band of 5 to 10 Hz. Although the Z direction is nearly parallel to $\tilde{\mathbf{B}}$, since $\tilde{\mathbf{B}}/\tilde{B}$ is significant (up to 10%), \tilde{E}_z does not represent E_{\parallel} . (h) E_{\parallel} at in the frequency range from DC to ~ 3.2 kHz. E_{\parallel} reaches over 100 mV/m peaks. (i) \tilde{J}_z in the frequency band from 5 to 10 Hz. (j) The energy exchange between fields and particles, $\mathbf{J} \cdot (\mathbf{E} + \mathbf{V}_e \times \mathbf{B})$, from DC to ~ 12 Hz. (k) A diagram of the current sheet adjacent to an EDR. The thin part of the current sheet is near the EDR. The drift waves appear to be confined in X and Z. (l) A magnified view of the large-amplitude E_{\parallel} Event 1. The signal is consistent with a nonlinear ion-acoustic wave. (m) The potential of the wave in Event 1 assuming that it is traveling at the ion-acoustic speed. (n) A magnified view of the large-amplitude E_{\parallel} Event 2. The signal is consistent with a nonlinear ion-acoustic wave. (o) The potential of the wave in Event 2 assuming that it is traveling at the ion-acoustic speed. In the Z = 0 plane, the wave consists of a set of alternating electron vortices as depicted in Figure 1. \mathbf{B} alternately twists clockwise and counter clockwise. The twisting of \mathbf{B} has a finite extent in Z. (q) A clockwise electron vortex (counterclockwise current) increases \mathbf{B} . The perpendicular electric field must be radially outward, resulting in a positive potential in the center. Since the twisting has a finite extent in Z, \tilde{E}_z must be finite. A counter clockwise electron current has a negative potential in the center.

Five vertical dashed lines mark the peaks and valleys of \tilde{B}_z (Figure 4c). Using these lines of reference, one can see that \tilde{P}_{ezz} , \tilde{P}_{exz} , \tilde{E}_z , \tilde{J}_z , and $\mathbf{J} \cdot (\mathbf{E} + \mathbf{V}_e \times \mathbf{B})$ have a role in the drift wave.

3.2. Parallel Potential

Figure 4k is an X - Z view of the confined drift wave. Figures 4l–4o are expanded views of the large-amplitude E_{\parallel} signals and integrated potentials. Figure 4p is a cartoon that is consistent with the observations and depicts the response of \mathbf{B} and \tilde{J}_z to the electron vortical motion. In this model, the twisting of \mathbf{B} is generated by electron vortical motion in the X - Y plane at $Z = 0$ (the region of the thin current sheet) and is confined along $\pm Z$. In this drawing, we assume that $Z = 0$ represents a node at which the drift wave is driven. In the $Z = 0$ plane, the electrons alternatively travel clockwise (blue circle) then counterclockwise (red circle) as discussed in section 3. It is important to note that the radial electric fields (\tilde{E}_x and \tilde{E}_y) reverse (as they must) when the electron vortical motion reverses, causing a positive potential in the center of the vortex during clockwise motion and a negative potential during the counterclockwise motion. The potential can be estimated as $|\tilde{E}_y|/|k_y| \approx 60$ V.

There are several numerical tests that one can perform on this 3-D model. The reversing of \tilde{E}_x and \tilde{E}_y along \mathbf{B} either creates a finite $\nabla \times \mathbf{E}$ and/or generates a finite \tilde{E}_z as depicted by the dashed orange square called the “Faraday Loop” in Figure 4q. Examining the X component of Faraday’s law,

$$ik_y \tilde{E}_z - \frac{\partial \tilde{E}_y}{\partial z} = i\omega \tilde{B}_x, \quad (28)$$

we can conclude that there must be a finite $\partial \tilde{E}_y / \partial z$ since $|k_y \tilde{E}_z| \gg |\omega \tilde{B}_x|$ in the observations.

We can crudely estimate $\partial \tilde{E}_y / \partial z$ from observations (14 December 2015 event) by examining the data from MMS3 and MMS4, which crossed the current sheet 0.43 and 0.54 s after MMS1. Figure 5 plots, in order, \mathbf{B} , n , \tilde{B}_z , \tilde{n}_e , \tilde{E}_x , \tilde{E}_y , \tilde{J}_x , and \tilde{J}_y in identical format as in Figure 1 from MMS3 (left side) and MMS4 (right side). MMS3 observations (Figure 5 left) see a similar drift wave as does MMS1 (Figure 1) with similar properties. MMS4 (Figure 5 right), however, reports significantly smaller amplitude oscillations in the 5- to 10-Hz frequency band. MMS4 was separated from MMS3 primarily in the Z direction by ~ 16 km (Figure 5q), which supports that the drift wave is confined in Z on the order of 16 km. Using the MMS1 observations ($|\tilde{E}_z| \approx 4$ mV/m, $|\tilde{E}_y| \approx 9$ mV/m, $|\tilde{B}_z| \approx 1$ nT, $k_y \approx 1.5 \times 10^{-4} \text{ m}^{-1}$) and assuming the Z distance is ~ 16 km, we get

$$|k_y \tilde{E}_z| \approx 6 \times 10^{-7} \frac{\text{V}}{\text{m}^2}, \quad \left| \frac{\partial \tilde{E}_y}{\partial z} \right| \approx 6 \times 10^{-7} \frac{\text{V}}{\text{m}^2}, \quad \text{and} \quad |\omega \tilde{B}_x| \approx 5 \times 10^{-8} \frac{\text{V}}{\text{m}^2} \quad (29)$$

Therefore, the observations support that $|k_y \tilde{E}_z|$ offsets $|\partial \tilde{E}_y / \partial z|$, which lends credence to the model of the drift wave and the confinement in the Z direction.

The Faraday Loop in Figure 4q also indicates that there must be ~ 60 V potential in the Z direction, which is nearly parallel to \mathbf{B} . The parallel electric field, on average, must be ~ 4 mV/m as well. The full bandwidth observations (Figure 4h) indicate spiky, large-amplitude (> 100 mV/m) E_{\parallel} events that are roughly phased with the drift wave. A close examination of the E_{\parallel} signals (Figures 4l and 4n) suggest large-amplitude, non-linear ion-acoustic waves. Assuming that these waves travel along \mathbf{B} at the ion-acoustic speed, the potential carried by these structures are ~ 10 to ~ 40 V, which is in consort with the estimated parallel potential.

A parallel potential requires either an electron inertial response or an electron pressure gradient:

$$m_e n_e \frac{\partial V_{\text{ell}}}{\partial t} + m_e n_e (\mathbf{V}_e \cdot \nabla) V_{\text{ell}} = -en_e E_{\parallel} - \left(\nabla \cdot \bar{\mathbf{P}}_e \right)_{\parallel} \quad (30)$$

where $\bar{\mathbf{P}}_e$ is the electron pressure tensor. One can quickly determine from the observations that the inertial terms on the left-hand side of equation (30) are small, so

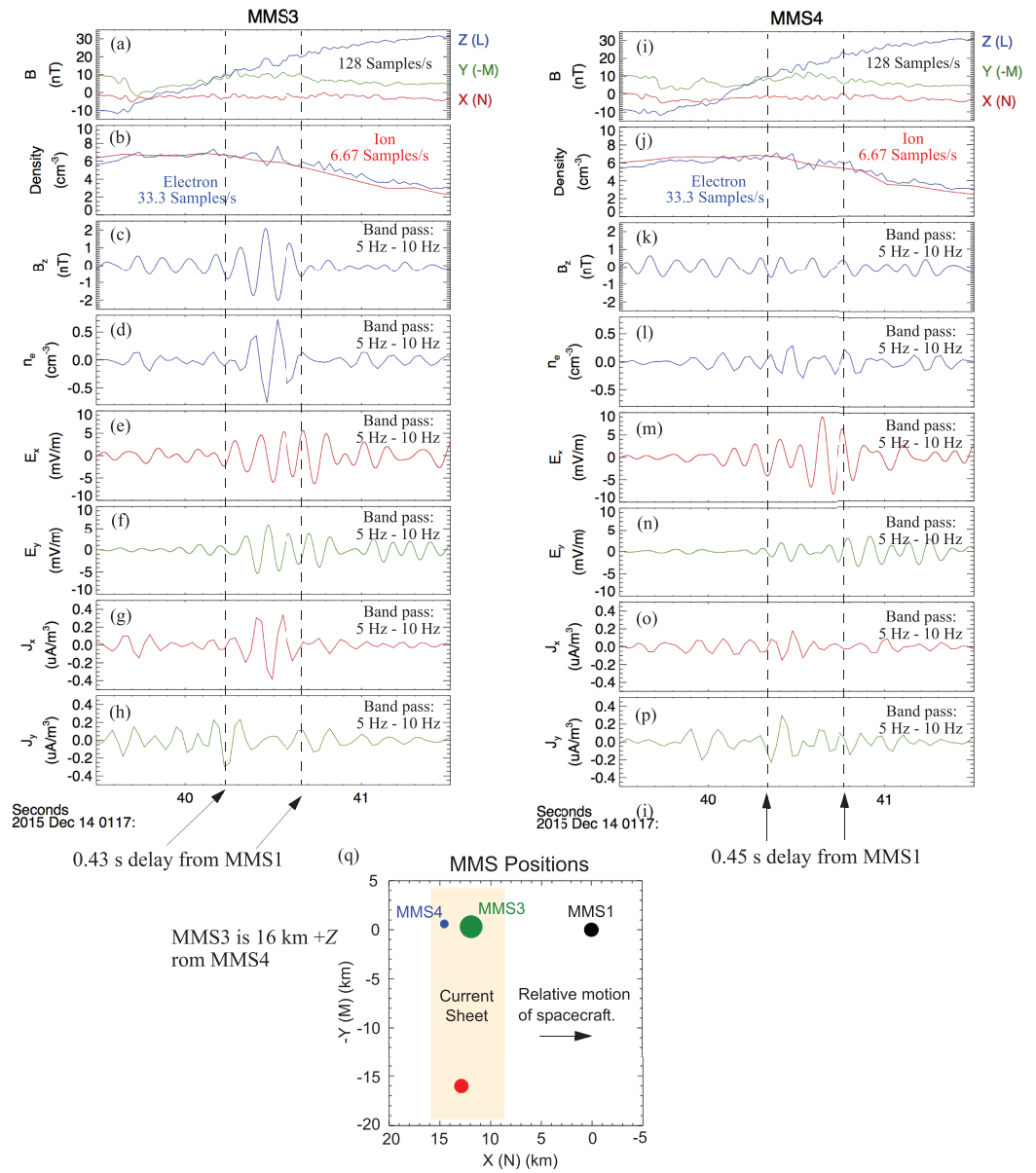


Figure 5. Observations of an electromagnetic drift wave from two spacecraft separated primarily in Z . (a–h) \mathbf{B} , n , \tilde{B}_z , \tilde{n}_e , \tilde{E}_x , \tilde{E}_y , \tilde{J}_x , and \tilde{J}_y from MMS3. (i–p) \mathbf{B} , n , \tilde{B}_z , \tilde{n}_e , \tilde{E}_x , \tilde{E}_y , \tilde{J}_x , and \tilde{J}_y from MMS4. MMS4 does not see an enhancement in \tilde{B}_z as it crossed the current sheet indicating that the drift wave has a finite extent along Z . (q) The relative positions of the MMS spacecraft.

$$\tilde{E}_{\parallel} = -\frac{(\nabla \cdot \tilde{\mathbf{P}}_e)_{\parallel}}{n_e e} = -\frac{1}{n_e e} \left(\frac{\partial \tilde{P}_{exz}}{\partial x} + \frac{\partial \tilde{P}_{eyz}}{\partial y} + \frac{\partial \tilde{P}_{ezz}}{\partial z} \right) \quad (31)$$

Figure 4e indicates that $|\tilde{P}_{ezz}| \approx 12$ pPa, $|\tilde{P}_{eyz}| \approx 6$ pPa (not shown), $|\tilde{P}_{exz}| \approx 8$ pPa (Figure 4f), and Figure 4b indicates that $n_e \approx 5 \text{ cm}^{-3}$. We can crudely determine how the parallel electric field is balanced using the scale lengths of the drift wave, $\delta z \sim 16$ km and $\delta x \sim 10$ km

$$|\tilde{E}_{\parallel}| \approx 4 \frac{\text{mV}}{\text{m}}; \left| \frac{1}{n_e e} \frac{\partial \tilde{P}_{exz}}{\partial x} \right| \approx 1 \frac{\text{mV}}{\text{m}}; \left| \frac{k_y \tilde{P}_{eyz}}{n_e e} \right| \approx 1 \frac{\text{mV}}{\text{m}}; \text{ and } \left| \frac{1}{n_e e} \frac{\partial \tilde{P}_{ezz}}{\partial z} \right| \approx 1 \frac{\text{mV}}{\text{m}} \quad (32)$$

which, given the uncertainties, corroborates that an electron pressure gradient can support \tilde{E}_{\parallel} in this wave. Interestingly, the off-diagonal terms appear to play a major role.

A primary conclusion of this analysis is that a 3-D model that incorporates an inhomogeneous background plasma is required to adequately describe the highly confined drift waves that potentially influence the electron diffusion region (EDR) of magnetic reconnection. A description of \mathbf{B} , \mathbf{E} , \mathbf{J} , and n require electron vortices and subsequent twisting of the \mathbf{B} . This model also explains the apparent discrepancy between the wavelength calculations from Faraday's law and that from Ampère's law. Near $Z = 0$ in Figure 4p, $|\tilde{B}_y|$ and $|\tilde{B}_x|$ are expected to be small but the curvature of the magnetic field line is at its maximum. Therefore, $\partial\tilde{B}_y/\partial z$ can make a substantial contribution to Ampère's law.

4. Wave Growth

The general drift instability (Krall & Liewer, 1971) describes a process under which a current sheet is unstable to lower hybrid or ion-acoustic waves. The LHDI (Davidson et al., 1977; Davidson & Gladd, 1975) furthers this work by concentrating on the impact of the electron drift from ∇P_e to generate wave growth. Lower hybrid waves may also be generated via a modified two-stream instability (McBride et al., 1972; Wu et al., 1983) involving a cross-field current. The observations of the drift waves point to the cross-field current (primarily from the electron drift) as the source of energy, in this case driven by E_x (normal electric field), which, in turn, is generated by a sharp ∇P_i .

It has been generally believed that the LHDI is ineffective with significant k_z . The analysis by Ji et al. (2004, 2005), however, has demonstrated that electromagnetic drift waves can be generated with a finite parallel propagation if electron Landau damping can be neglected. Even though Ji et al. (2004, 2005) did not address the strong inhomogeneous plasma or incorporate an eigenmode treatment, we base our brief wave-growth discussion on this work.

Wave growth is generally derived by calculating the real and imaginary part of the plasma dielectric function and applying them to the particular wave dispersion. Such a calculation generally ignores inhomogeneity in \mathbf{B} and n and is very difficult to apply to an eigenmode structure. Here we take a more heuristic approach to wave growth by examining $\mathbf{J} \cdot (\mathbf{E} + \mathbf{V}_e \times \mathbf{B})$.

There are several important clues in the observations on the wave growth. One noticeable feature is that $v_{\phi} \sim v_{thi}$, so the ions can exchange energy with the wave through Landau resonance. In the ion frame, the ions should gain energy in this interaction (wave damping) since the ion distribution (f_i) is observed to be stable ($\partial f_i / \partial v < 0$). The primary energy exchange will be through \tilde{E}_y , which is similar to that reported by analyses of the LHDI (Davidson et al., 1977; Davidson & Gladd, 1975) and by Ji et al. (2004, 2005). Even though the energy exchange with ions directly acts to damp the wave, the ion energy exchange may lead to a possible momentum exchange with electrons. If so, the electron energy loss could greatly exceed the ion energy gain leading to wave growth.

A finite energy exchange between the drift wave and electrons requires that $\mathbf{J} \cdot (\mathbf{E} + \mathbf{V}_e \times \mathbf{B}) \neq 0$. The general model of the drift wave called for frozen-in electron motion. However, if we rearrange the electron force equation as follows:

$$\mathbf{E} + \mathbf{V}_e \times \mathbf{B} = -\frac{m_e \partial \mathbf{V}_e}{e \partial t} - \frac{m_e (\mathbf{V}_e \cdot \nabla) \mathbf{V}_e}{e} - \frac{\nabla \cdot \bar{\mathbf{P}}_e}{en_e} \quad (33)$$

one can see that a finite energy exchange between the drift wave and electrons requires a finite electron pressure gradient or acceleration. Again, we use the observations to guide us. The values of the first two terms on the right-hand side of equation (33) can be shown to be small compared to the pressure gradients (Figures 4e and 4f). Except in the description of the parallel motions, electron pressure gradients are primarily ignored in the wave model. They, however, should not be ignored when considering wave growth.

Figure 4j shows a powerful energy exchange $\mathbf{J} \cdot (\mathbf{E} + \mathbf{V}_e \times \mathbf{B})$ that is coincident with the drift wave and in the same frequency range. The average value of $\mathbf{J} \cdot (\mathbf{E} + \mathbf{V}_e \times \mathbf{B})$ could indicate wave growth or damping, which, in this example, indicates growth since $\mathbf{J} \cdot (\mathbf{E} + \mathbf{V}_e \times \mathbf{B}) < 0$. Wave growth or damping, of course, depends on

the stage of evolution of the drift wave, so one cannot draw solid conclusions. However, quantitatively, Figure 4j suggests that $\mathbf{J} \cdot (\mathbf{E} + \mathbf{V}_e \times \mathbf{B})$ could conceivably be on the order of ~ -1 nW/m³ during the peak growth phase of the wave. Even though the drift wave has a dominant electrostatic component, the wave energy is dominated by $\tilde{\mathbf{B}}$:

$$W_B \approx \frac{\tilde{\mathbf{B}}^2}{8\mu_0} \quad (34)$$

Setting $\tilde{\mathbf{B}}$ to 2 nT, $W_B \sim 0.4$ pW/m³, the wave growth (or damping) rate from $\mathbf{J} \cdot (\mathbf{E} + \mathbf{v}_e \times \mathbf{B})$ can be

$$\frac{1}{W_B} \frac{\partial W_B}{\partial t} \approx \frac{\mathbf{J} \cdot (\mathbf{E} + \mathbf{v}_e \times \mathbf{B})}{W_B} \approx O(10^3) \text{ s}^{-1}, \quad (35)$$

which demonstrates that there is ample energy exchange for wave growth and damping.

5. Summary

This analysis is repeated for five other examples of drift wave observations, three of which are presented in the *companion paper*. The common themes in these observations are listed below.

1. Electromagnetic drift waves appear in thin, Hall current sheets near the EDR which have a significant normal electric field (\bar{E}_x) that offsets a strong ion pressure gradient (∇P_i). \bar{E}_x is responsible for the driving strong electron flow, which, in turn, carries the primary current of the current sheet.
2. In the ion frame, the drift waves propagate along the X line of magnetic reconnection in the $-Y$ ($+M$) direction. The wavelengths are less than ρ_i and greater than ρ_e , often ~ 50 km in the Earth's magnetopause. The drift waves are narrowly confined in the X direction (surface normal) to the region of strong electron current (the current sheet). The perpendicular confinement (L_x) is such that $L_x \leq \lambda$. They are also confined parallel to \mathbf{B} (Z or L direction) in the region of the strongest electron current.
3. Since the waves are confined to the current sheet, the background plasma is strongly varying. The waves often appear where $\partial B_z / \partial x < 0$ and $\partial n_e / \partial x > 0$.
4. The condition $\partial B_z / \partial x < 0$ and $\partial n_e / \partial x > 0$ promotes the wave to appear as a corrugation of the current sheet, as demonstrated in the *companion paper* and in equations (14) and (24). The displacement of the current sheet can reach >5 km in the examples shown, which is a significant fraction of L_x .
5. In the plane perpendicular to \mathbf{B} , the drift waves appear as a series of alternating vortices in the electron flow. The alternating vortices are consistent with the fluctuations in $|\mathbf{B}|$ and n_e . The vortices also have alternating center potentials.
6. Perpendicular ion motion requires kinetic treatment. The drift waves propagate at a speed near the ion thermal speed, which should produce a strong Landau resonance. The ions are plowed back and forth in the surface normal direction from a combination of E_x motion and amplitude modulation of E_x . The ion motion in the normal direction is critical to maintaining a quasi-neutral plasma.
7. It is essential to consider the parallel behavior of the drift waves. Because electrons are primarily frozen in, the electron vortices twist \mathbf{B} alternately clockwise and counterclockwise. The twisting action in the center of the current sheet causes substantial $\partial B_y / \partial x$ and $\partial B_x / \partial y$ which, in addition to the fluctuations in B_z , are self-consistent with perpendicular currents.
8. A parallel electric field arises in the drift waves due to the alternating potentials in the perpendicular plane and the finite extent along \mathbf{B} . \tilde{E}_{\parallel} , as observed, is highly localized and spiky. On average, it is supported by a combination of direct electron pressure fluctuations and gradients in the off-diagonal electron pressure terms. The off-diagonal terms allow the Z momentum from \tilde{E}_{\parallel} to be transported in the X and Y directions and vice versa. Clearly, the drift waves must be treated in 3-D.
9. Wave growth may be similar to that of the LHDI but must include eigenmode analysis (e.g., Daughton et al., 2004) and the parallel behavior (e.g., Ji et al., 2004, 2005). Treatments that are solely based on classical lower hybrid waves are unlikely to be adequate.
10. The observations of $\mathbf{J} \cdot (\mathbf{E} + \mathbf{V}_e \times \mathbf{B})$ show a strong energy exchange, primarily with electrons. This energy exchange is mostly oscillatory. However, a small negative bias could readily explain wave growth.

11. Because the ions are Landau resonant and the electron show strong energy exchange, wave growth is likely from the strong, perpendicular electron-ion drift (Krall & Liewer, 1971). The current supporting the current sheet is generated by electron drift from E_x , which, in turn, is supported by ∇P_i . Ultimately, the energy source is likely from the ion pressure gradient.
12. If the wave growth is as suggested, the drift wave may promote a significant momentum exchange between ions and electrons in the current sheet.

6. Conclusions

We have presented a 3-D model of electromagnetic drift waves that are observed immediately adjacent to the electron diffusion region of magnetic reconnection. The waves travel in the $-Y (+M)$ direction and appear to consist of a series of electron vortices alternating in sense from clockwise to counterclockwise. Small-scale electron flow vortices are seen in simulations (e.g., Price et al., 2016; Price et al., 2017) and are associated with a shear in electron flow. The electron current, in turn, modulates the amplitude of B_z . When the electron vortex is clockwise, the electric field is radially outward indicating a positive potential in the center of the vortex. When electron vortex is counterclockwise, the potential in the center is negative. The vortical motion of the electron twists \mathbf{B} alternately clockwise and counterclockwise, which propagate in the Z direction. The drift waves also appear to be confined in the Z direction, so the resulting flux ropes are near the EDR.

The electron density perturbation (\tilde{n}_e) is primarily from motion in the X direction combined with a steep gradient in n_o , so $\tilde{n}_e \propto \tilde{V}_{ex} \partial n_o / \partial x$. We also demonstrated that $\tilde{B}_z \propto \tilde{V}_{ex} \partial \bar{B}_z / \partial x$. These two relations imply a physical corrugation of the current sheet with a displacement in the X direction.

\tilde{E}_y is confined in the X and Z directions with sinusoidal variation in the Y direction (along the reconnection X line). \bar{E}_x is sharply peaked in the center of the current sheet. \tilde{E}_x develops from a combination of displacement of \bar{E}_x in the X direction, amplitude modulation, and possibly a change in shape. Since $v_\phi \approx v_{thi}$, the ion motion in the Y direction is expected to have a strong Landau resonance. The ion motion in the X direction appears to come from \bar{E}_x “plowing” the ions back and forth and appears to be the main driver of \tilde{n}_i to maintain quasineutrality.

The empirical model has many of the characteristics of modes predicted by Daughton et al. (2004), who describes a confined eigenmode in a thin current sheet generated through the LHDI. The observed waves differ in that they are more strongly confined in the X direction (surface normal) and are also confined in the Z direction (along \mathbf{B}). The observations also are in consort with the electromagnetic drift waves observed in laboratory magnetic reconnection experiments (Ji et al., 2004, 2005). The latter work showed that drift waves with finite k_z could grow. A similar mode also appears in 3-D numerical simulations (Price et al., 2016, 2017), who conclude that the drift waves develop from the LHDI, but the authors cautioned that there are significant differences. As such, it is possible that the observed electromagnetic drift waves may be connected to a branch of the classical LHDI. The growth process is analogous. However, the strong confinement in X and Z , the kinetic ion behavior, and the 3-D properties call for a theoretical treatment that goes beyond the classical LHDI (Ergun et al., 2017).

Electromagnetic drift waves are potentially important since they appear to corrugate the current sheet near the EDR and, in doing so, can displace the X line. Asymmetric magnetic reconnection at the magnetopause is such that the stagnation point, which is part of the EDR, can be in the current sheet that carries the drift waves (Burch, Moore, et al., 2016; Hesse et al., 2014). In one example (Figure 6 in the *companion paper*), the drift waves reach nonlinear amplitudes ($|\tilde{\mathbf{B}}| \sim |\mathbf{B}|$, $|\tilde{n}_e| \sim |n_e|$) which can potentially impact the magnetic reconnection process by generating turbulence that results in patchy magnetic reconnection. The magnetic response in a drift wave is a combination of localized enhancements in $|\mathbf{B}|$ and a series of flux ropes alternating in sense. In the nonlinear stage of evolution, independent, small-scale flux, ropes may form. Observations often show that \mathbf{B} is highly variable near the magnetic reconnection regions at the Earth’s magnetopause indicating 3-D structure. The drift waves as observed and described may play a principal role in this variability.

Acknowledgments

The authors thank the MMS team for their extraordinary effort in making the mission a success. The authors thank Cecilia Norgren for her useful discussions. This article is supported by the NASA MMS mission. All data used in this article are publicly available at <https://lasp.colorado.edu/mms/sdc/public/> website.

References

- Burch, J. L., Moore, T. E., Torbert, R. B., & Giles, B. L. (2016). Magnetospheric multiscale overview and science objectives. *Space Science Reviews*, 199, 5–21. <https://doi.org/10.1007/s11214-015-0164-9>
- Burch, J. L., Torbert, R. B., Phan, T. D., Chen, L.-J., Moore, T. E., Ergun, R. E., et al. (2016). Electron-scale measurements of magnetic reconnection in space. *Science*. <https://doi.org/10.1126/science.aaf2939>
- Cassak, P. A., & Shay, M. A. (2007). Scaling of asymmetric magnetic reconnection: General theory and collisional simulations. *Physics of Plasmas*, 14, 102114. <https://doi.org/10.1063/1.2795630>
- Chen, L.-J., Hesse, M., Wang, S., Gershman, D., Ergun, R. E., Burch, J., et al. (2017). Electron diffusion region during magnetopause reconnection with an intermediate guide field: Magnetospheric Multiscale observations. *Journal of Geophysical Research: Space Physics*, 122, 5235–5246. <https://doi.org/10.1002/2017JA024004>
- Daughton, W. (2003). Electromagnetic properties of the lower-hybrid drift instability in a thin current sheet. *Physics of Plasmas*, 10(8), 3103–3119. <https://doi.org/10.1063/1.1594724>
- Daughton, W., Lapenta, G., & Ricci, P. (2004). Nonlinear evolution of the lower-hybrid drift instability in a current sheet. *Physical Review Letters*, 93(10), 105004. <https://doi.org/10.1103/PhysRevLett.93.105004>
- Daughton, W., Roytershteyn, V., Karimabadi, H., Yin, L., Albright, B. J., Bergen, B., & Bowers, K. J. (2011). Role of electron physics in the development of turbulent magnetic reconnection in collisionless plasmas. *Nature Physics*, 7(7), 539–542. <https://doi.org/10.1038/nphys1965>
- Davidson, R., Gladd, N., Wu, C., & Huba, J. (1977). Effects of finite plasma beta on the lower-hybrid drift instability. *Physics of Fluids*, 20, 301. <https://doi.org/10.1063/1.861867>
- Davidson, R. C., & Gladd, N. T. (1975). Anomalous transport properties associated with the lower-hybrid-drift instability. *Physics of Fluids*, 18, 1327–1335. <https://doi.org/10.1063/1.861021>
- Denton, R. E., Sonnerup, B. U. Ö., Russell, C. T., Hasegawa, H., Phan, T.-D., Strangeway, R. J., et al. (2018). Determining L-M-N current sheet coordinates at the magnetopause from Magnetospheric Multiscale data. *Journal of Geophysical Research: Space Physics*, 123, 2274–2295. <https://doi.org/10.1002/2017ja024619>
- Eastwood, J. P., Phan, T. D., Bale, S. D., & Tjulin, A. (2009). Observations of turbulence generated by magnetic reconnection. *Physical Review Letters*, 102, 035001. <https://doi.org/10.1103/physrevlett.102.035001>
- Ergun, R. E., Chen, L.-J., Wilder, F. D., Ahmadi, N., Eriksson, S., Usanova, M. E., et al. (2017). Drift waves, intense parallel electric fields, and turbulence associated with asymmetric magnetic reconnection at the magnetopause. *Geophysical Research Letters*, 44, 2978–2986. <https://doi.org/10.1002/2016GL072493>
- Ergun, R. E., Hoilijoki, S., Ahmadi, N., Schwartz, S. J., Wilder, F. D., Burch, J. L., et al. (2019). Magnetic Reconnection in Three Dimensions: Observations of Electromagnetic Drift Waves in the Adjacent Current Sheet. *Journal of Geophysical Research: Space Physics*, 124. <https://doi.org/10.1029/2019JA027228>
- Ergun, R. E., Holmes, J. C., Goodrich, K. A., Wilder, F. D., Stawarz, J. E., Eriksson, S., et al. (2016). Magnetospheric Multiscale observations of large amplitude, parallel, electrostatic waves associated with magnetic reconnection at the magnetopause. *Geophysical Research Letters*, 43, 5626–5634.
- Ergun, R. E., Tucker, S., Westfall, J., Goodrich, K. A., Malaspina, D. M., Summers, D., et al. (2016). The axial double probe and fields signal processing for the MMS mission. *Space Science Reviews*, 199(1-4), 167–188. <https://doi.org/10.1007/s11214-014-0115-x>
- Fried, B. D., & Conte, S. D. (1961). *The Plasma Dispersion Function*. San Diego, CA: Academic Press.
- Graham, D. B., Khotyaintsev, Y. V., Norgren, C., Vaivads, A., André, M., Toledo-Redondo, S., et al. (2017). Lower hybrid waves in the ion diffusion and magnetospheric inflow regions. *Journal of Geophysical Research: Space Physics*, 122, 517–533. <https://doi.org/10.1002/2016ja023572>
- Hesse, M., Aunai, N., Sibeck, D., & Birn, J. (2014). On the electron diffusion region in planar, asymmetric, systems. *Geophysical Research Letters*, 41(24), 8673–8680. <https://doi.org/10.1002/2014GL061586>
- Huba, J. D., Gladd, N. T., & Papadopoulos, K. (1977). The lower-hybrid-drift instability as a source of anomalous resistivity for magnetic field line reconnection. *Geophysical Research Letters*, 4, 125–128. <https://doi.org/10.1029/gl004i003p00125>
- Ji, H., Kulsrud, R., Fox, W., & Yamada, M. (2005). An obliquely propagating electromagnetic drift instability in the lower hybrid frequency range. *Journal of Geophysical Research*, 110, A08212. <https://doi.org/10.1029/2005JA011188>
- Ji, H., Terry, S., Yamada, M., Kulsrud, R., Kuritsyn, A., & Ren, Y. (2004). Electromagnetic fluctuations during fast reconnection in a laboratory plasma. *Physical Review Letters*, 92, 115001. <https://doi.org/10.1103/physrevlett.92.115001>
- Karimabadi, H., Daughton, W., & Scudder, J. (2007). Multi-scale structure of the electron diffusion region. *Geophysical Research Letters*, 34, L13104. <https://doi.org/10.1029/2007GL030306>
- Krall, N. A., & Liewer, P. C. (1971). Low-frequency instabilities in magnetic pulses. *Physical Review A*, 4(5), 2094. <https://doi.org/10.1103/PhysRevA.4.2094>
- Lapenta, G., Krauss-Varban, D., Karimabadi, H., Huba, J. D., Rudakov, L. I., & Ricci, P. (2006). Kinetic simulations of x-line expansion in 3D reconnection. *Geophysical Research Letters*, 33, L10102. <https://doi.org/10.1029/2005GL025124>
- Le, A., Daughton, W., Ohia, O., Chen, L.-J., Liu, Y.-H., Wang, S., et al. (2018). Drift turbulence, particle transport, and anomalous dissipation at the reconnecting magnetopause. *Physics of Plasmas*, 25(6), 062103. <https://doi.org/10.1063/1.5027086>
- Le Contel, O., Leroy, P., Roux, A., Coillot, C., Alison, D., Bouabdellah, A., et al. (2016). The search-coil magnetometer for MMS. *Space Science Reviews*, 199(1-4), 257–282. <https://doi.org/10.1007/s11214-014-0096-9>
- Le Contel, O., Retinò, A., Breuillard, H., Mirioni, L., Robert, P., Chasapis, A., et al. (2016). Whistler mode waves and hall fields detected by MMS during a dayside magnetopause crossing. *Geophysical Research Letters*, 43, 5943–5952. <https://doi.org/10.1002/2016GL068968>
- Lindqvist, P.-A., Olsson, G., Torbert, R. B., King, B., Granoff, M., Rau, D., et al. (2016). The spin-plane double probe instrument for MMS. *Space Science Reviews*, 199(1-4), 137–165. <https://doi.org/10.1007/s11214-014-0116-9>
- Malakit, K., Shay, M. A., Cassak, P. A., & Ruffolo, D. (2013). New electric field in asymmetric magnetic reconnection. *Physical Review Letters*, 111(13), 135001. <https://doi.org/10.1103/PhysRevLett.111.135001>
- McBride, J., Ott, E., Boris, J., & Orens, J. (1972). Theory and simulation of turbulent heating by the modified two-stream instability. *Physics of Fluids*, 15(12), 2367.
- Nakamura, T. K. M., Nakamura, R., Narita, Y., Baumjohann, W., & Daughton, W. (2016). Multi-scale structures of turbulent magnetic reconnection. *Physics of Plasmas*, 23(5), 052116. <https://doi.org/10.1063/1.4951025>
- Norgren, C., Vaivads, A., Khotyaintsev, Y. V., & Andre, M. (2012). Lower hybrid drift waves: Space observations. *Physical Review Letters*, 109(5), 055001. <https://doi.org/10.1103/PhysRevLett.109.055001>

- Pollock, C., Moore, T., Jacques, A., Burch, J., Gliese, U., Saito, Y., et al. (2016). Fast plasma investigation for Magnetospheric Multiscale. *Space Science Reviews*, *199*, 331–406. <https://doi.org/10.1007/s11214-016-0245-4>
- Price, L., Swisdak, M., Drake, J. F., Burch, J. L., Cassak, P. A., & Ergun, R. E. (2017). Turbulence in three-dimensional simulations of magnetopause reconnection. *Journal of Geophysical Research: Space Physics*, *122*, 11,086–11,099. <https://doi.org/10.1002/2017JA024227>
- Price, L., Swisdak, M., Drake, J. F., Cassak, P. A., Dahlin, J. T., & Ergun, R. E. (2016). The effects of turbulence on three-dimensional magnetic reconnection at the magnetopause. *Geophysical Research Letters*, *43*, 6020–6027. <https://doi.org/10.1002/2016GL069578>
- Pritchett, P. L., Mozer, F. S., & Wilber, M. (2012). Intense perpendicular electric fields associated with three-dimensional magnetic reconnection at the subsolar magnetopause. *Journal of Geophysical Research*, *117*, A06212. <https://doi.org/10.1029/2012JA017533>
- Roytershteyn, V., Daughton, W., Karimabadi, H., & Mozer, F. S. (2012). Influence of the lower-hybrid drift instability on magnetic reconnection in asymmetric configurations. *Physical Review Letters*, *108*, 185001. <https://doi.org/10.1103/PhysRevLett.108.185001>
- Roytershteyn, V., Dorfman, S., Daughton, W., Ji, H., & Yamada, M. (2013). Electromagnetic instability of thin reconnection layers: Comparison of three-dimensional simulations with MRX observations. *Physics of Plasmas*, *20*, 061212. <https://doi.org/10.1063/1.4811371>
- Russell, C. T., Anderson, B. J., Baumjohann, W., Bromund, K. R., Dearborn, D., Fischer, D., et al. (2016). The Magnetospheric Multiscale magnetometers. *Space Science Reviews*, *199*, 189–256. <https://doi.org/10.1007/s11214-014-0057-3>
- Torbert, R. B., Russell, C. T., Magnes, W., Ergun, R. E., Lindqvist, P.-A., LeContel, O., et al. (2016). The FIELDS instrument suite on MMS: Scientific objectives, measurements, and data products. *Space Science Reviews*, *199*, 105–135. <https://doi.org/10.1007/s11214-014-0109-8>
- Wilder, F. D., Ergun, R. E., Newman, D. L., Goodrich, K. A., Trattner, K. J., Goldman, M. V., et al. (2017). The nonlinear behavior of whistler waves at the reconnecting dayside magnetopause as observed by the magnetospheric multiscale mission: A case study. *Journal of Geophysical Research: Space Physics*, *122*, 5487–5501. <https://doi.org/10.1002/2017JA024062>
- Wu, C. S., Winske, D., Papadopoulos, K., Zhou, Y. M., Tsai, S. T., & Guo, S. C. (1983). A kinetic cross-field streaming instability. *Physics of Fluids*, *26*, 1259–1267. <https://doi.org/10.1063/1.864285>